Vacuum 178 (2020) 109434

Contents lists available at ScienceDirect

Vacuum

journal homepage: http://www.elsevier.com/locate/vacuum

Structural and optical properties of Si hyperdoped with Te by ion implantation and pulsed laser annealing

Fadei F. Komarov [a,b], Nikita S. Nechaev [c], Gennadii D. Ivlev [c], Liudmila A. Vlasukova [c], Irina N. Parkhomenko [c], Elke Wendler [d,*], Ivan A. Romanov [c], Yonder Berencén [e], Vladimir V. Pilko [a], Dmitrii V. Zhigulin [c], Alexander F. Komarov [a]

[a] *A.N. Sevchenko Institute of Applied Physical Problems of Belarusian State University, 220045, Minsk, Kurchatov Str 7, Belarus*
[b] *National University of Science and Technology MISIS, 119049, Moscow, Leninskiy Ave, 4, Russian Federation*
[c] *Belarusian State University, 220030, Minsk, Nezavisimosty Ave 4, Belarus*
[d] *Friedrich-Schiller-Universität, D07743, Max-Wien-Platz 1, Jena, Germany*
[e] *Helmholtz-Zentrum Dresden-Rossendorf, Institute of Ion Beam Physics and Materials Research, Bautzner Landstr.400, 01328, Dresden, Germany*

ARTICLE INFO

Keywords:
IR photodetectors
Te-hyperdoped silicon
Ion implantation
Pulsed laser annealing
Absorption spectra

ABSTRACT

Structural and absorption properties of Te-implanted silicon layers after pulsed laser melting, equilibrium furnace annealing and rapid thermal annealing were examined and compared. The advantage of laser annealing in the formation of absorbing silicon-based layers is demonstrated. Silicon layers doped with Te up to concentrations of (3–5) × 10^{20} cm^{-3} were formed via ion implantation and pulsed laser melting. It is found that 70–90% of the embedded impurity atoms are in substitutional states in the silicon lattice. A significant increase of the absorption (to 35–65%) in the wavelength range of 1100–2500 nm is obtained, which is useful for Si-based photodiodes. The effect of energy density of the laser pulse on the structural and optical properties of Te-hyperdoped silicon is discussed. The current-voltage characteristics and the photosensitivity of Te-doped silicon photodiodes are investigated.

1. Introduction

Silicon (Si) is the fundamental material of microelectronics, but it is considered to have limited applications for optoelectronics. Due to the relatively large band gap (1.12 eV) silicon is not able to absorb electromagnetic radiation of wavelength longer than 1100 nm. The consequence is the transmission of light in silicon solar cells in the infrared (IR) part of the solar spectrum at about 1.1–3 μm and an ineffective functioning of silicon photodetectors at three main fiber-optic communications wavelength bands: S (1460–1.530 nm), C (1530–1565 nm) and L (1565–1625 nm) [1]. To solve these problems, researchers are also focusing on the creation of low-cost and efficient IR photodetectors compatible with the silicon complementary metal-oxide-semiconductor (CMOS) technology.

To date, it has been established that the highest absorption coefficient of light in the IR range at room temperature (~10^4 cm^{-1}) is observed for chalcogen (sulfur, selenium, tellurium (Te))-hyperdoped silicon [2]. The equilibrium chalcogen solubility in silicon is ~10^{16} cm^{-3}. Chalcogens create deep levels within the forbidden gap at such a level of concentrations. However, if the impurity concentration exceeds the equilibrium solubility limit by 4–5 orders of magnitude, the impurity levels form an impurity band. Then, photon absorption due to electron transitions 'valence band – impurity band' and 'impurity band – conduction band' becomes possible [3]. Impurity doping higher than the saturation threshold can be achieved by non-equilibrium methods, such as ion implantation followed by furnace annealing [4,5], femto-, pico-, nanosecond laser pulse [2] or flash lamp annealing [6].

In 1961, Shockley and Queisser showed that the theoretical efficiency limit of silicon solar cells is 41% [7]. Later, the authors of Ref. [8] showed that the theoretical efficiency limit of solar cells based on modified silicon with an impurity band is 63%. Thus, the maximal efficiency of solar cells based on chalcogen-hyperdoped silicon can be

---

* Corresponding author.
E-mail addresses: komarovf@bsu.by (F.F. Komarov), nsnechaev@gmail.com (N.S. Nechaev), ivlev@bsu.by (G.D. Ivlev), vlasukova@bsu.by (L.A. Vlasukova), parkhomenko@bsu.by (I.N. Parkhomenko), elke.wendler@uni-jena.de (E. Wendler), romivan@bsu.by (I.A. Romanov), y.berencen@hzdr.de (Y. Berencén), pilkowladimir@gmail.com (V.V. Pilko), komarovaf@bsu.by (A.F. Komarov).

https://doi.org/10.1016/j.vacuum.2020.109434
Received 5 March 2020; Received in revised form 23 April 2020; Accepted 24 April 2020

significantly enhanced in comparison with that obtained in conventional silicon ones.

Furthermore, it should be noted that further miniaturization of silicon devices demands ultrahigh concentrations of free electrons ~10^{21} cm^{-3} [9]. At present, a high concentration of free electrons is obtained by doping silicon with impurities that create shallow levels in the band gap of silicon (P, As and Sb). These impurities have a small activation energy (20–50 meV), a small diffusion coefficient, and a rather large solubility limit in silicon. However, it is not possible to obtain a free electron concentration above 5×10^{20} cm^{-3} even at the concentrations of “shallow levels” impurities higher the solubility limit [10]. Recently, it has been established that silicon doping with “deep-level” impurities (for example, chalcogens) can provide free electron concentrations above 10^{20} cm^{-3}. This process is associated with the so-called ‘insulator-metal’ transition implying overlap of the impurity band with the conduction band [11]. In this case, the concentration of free electrons increases linearly with increasing impurity concentration, while the fraction of electrically activated impurity atoms (located in the silicon lattice sites) remains almost unchanged [12]. In particular, according to Refs. [13] p-n photodiodes based on Te-hyperdoped silicon (with Te concentration ~10^{21} cm^{-3}) exhibit remarkable photoresponse over a broad spectral range at room temperature. Ref. [14] demonstrates that Te-hyperdoped silicon remains stable after heat treatment at 500 °C for 10 min. Therefore, such a material is perspective for future development of CMOS technology.

The present work is devoted to Te-hyperdoped silicon layers fabricated by ion implantation followed by furnace, rapid thermal and pulsed laser annealing. Our investigation focuses on the effect of different regimes of thermal treatment on structural and optical properties of Te-hyperdoped silicon layers. Additionally photodiode test structures are produced for studying the photoresponse of the Te-hyperdoped silicon layers.

2. Experimental

A double-side polished silicon (Si) (111) p-type wafer with an electrical resistivity of 10 Ω cm was implanted with 200 keV Te^+ with a fluence of 1×10^{16} $ions/cm^2$ at room temperature. The vacuum level in an ion accelerate chamber during ion implantation was 10^{-7} Torr. The implanted samples were annealed in a resistance furnace at 900 °C for 30 min and in a rapid thermal annealing (RTA) system (JetFirst 100) at 1200°C for 3 min in Ar atmoshere. Also pulsed laser annealing (PLA) of the implanted layers was carried out with an in-situ optical diagnostics of the phase transformations described in Ref. [15]. The as-implanted wafers were irradiated by a single pulse of a ruby laser (0.69 μm) in ambient air. Pulse energy densities W were set at 1.5, 2.0 and 2.5 J/cm^2.

The surface morphology of the implanted and annealed samples was studied using the scanning electron microscope Hitachi S-4800. Additionally, elemental composition was studied using the Brucker energy dispersive X-ray (EDX) analysis system. For more detailed analysis, Te depth distribution profiles, substitutional fraction of incorporated Te in Si lattice and crystallinity of the implanted and annealed Si samples were analyzed by Rutherford backscattering spectrometry in random (RBS/R) and channeling directions (RBS/C) using 1.4 MeV He^+ ions. The impurity concentration profiles were extracted from the RBS/R spectra with the help of the code SIMNRA [16] and compared with the calculated ones using the BEAM2HD code [17]. To investigate the crystalline quality of the modified silicon layers, Raman spectroscopy (RS) measurements were performed in backscattering geometry with a Ramanor U1000 (Jobin Yvon) spectrometer using a 532-nm laser beam as the excitation source at room temperature. Optical spectra (transmission and reflectance) were studied at room temperature in the spectral range of 250–2500 nm by means of Lambda 1050 spectrometer. Absorption spectra were calculated by the formula

$$A = 100\% - R - T. \tag{1}$$

3. Results and discussion

3.1. In-situ optical diagnostics during PLA

The as-implanted samples were irradiated with a single pulse of the ruby laser. The pulse was of nearly Gaussian temporal shape with the full width at a half maximum (FWHM) being 75 ns (Fig. 1a). The lifetime of the molten phase was determined by the method of time-resolved reflectivity (Fig. 1 b, c, d). For the realization of this method, the collimated beam of the second harmonic of a Nd-laser (λ = 0.53 μm) was focused on the centre of the laser irradiated zone at an incidence angle of 40°. Its intensity in the spot (~1 mm) was much lower than that of the annealing ruby laser pulse to avoid thermal destructive effects. The intensity of the beam reflected from the sample was detected by a photomultiplier. It is known that a relatively weak increase of the reflected beam intensity is observed during laser annealing at energy densities of the ruby laser pulse lower than 1 J/cm^2 [15]. It is caused by the temperature dependence of the optical parameters of crystalline Si. An ultrathin layer of the liquid phase appears on the sample surface at $W = 1$ J/cm^2 (melting threshold). Its thickness is less than the thickness of the skin layer (~10 nm). A significant increase of the reflection coefficient (2.5 times at λ = 0.53 μm) is registered when overcoming a laser energy density of $W = 1$ J/cm^2, which can be attributed to the existence of molten Si. Thus, the life-time of the liquid phase is determined by registration of the duration of the increased reflected signal. As can be seen from Fig. 1 b-d the life-time of the liquid phase enhances with increasing energy density. The time of phase transformation is equal to 190, 270 and 370 ns at laser melting induced by pulses with energy densities of 1.5 J/cm^2, 2.0 and 2.5 J/cm^2, respectively.

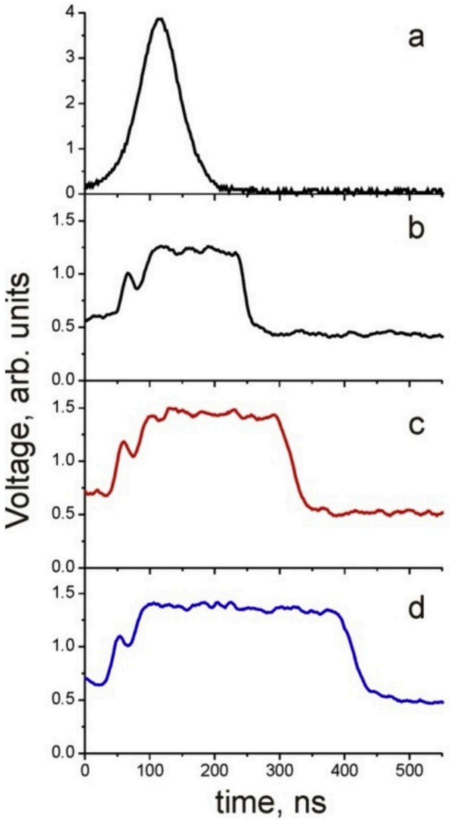

Fig. 1. Oscillograms of the photodetector output signals recording the ruby laser pulse (a) and the reflectivity (R) at 0.53 μm for the implanted Si during PLA at W 1.5 (b), 2.0 (c) and 2.5 J/cm^2 (d).

3.2. Structural and element composition

Fig. 2 shows the SEM micrographs of the implanted Si samples before and after different treatments. The surface of the as-implanted sample does not exhibit any structural peculiarities (Fig. 2a). The furnace annealing at 900 °C results in the formation of dark droplets assigned to Te segregation on the sample surface (Fig. 2b). The surface after RTA is rough and tuberous. A smooth surface morphology without any Te agglomerates on the surface is observed for the implanted samples after PLA (Fig. 2d, e, f). Only the sample after PLA at the highest energy density ($W = 2.5$ J/cm^2) exhibits insignificant surface irregularities.

EDX analysis (not shown here) reveals the presence of Te impurities in all implanted and annealed samples except the one after RTA. Apparently, the tuberous surface of this sample is caused by Te evaporation. The RBS analysis was used for a more detailed analysis of the depth distribution of implanted Te atoms. Fig. 3 shows the RBS spectra measured in random (R) and channeling (C) regimes. As can be seen from the figure, furnace annealing results in a significant Te diffusion towards the surface. PLA results in tellurium redistribution towards both the surface and into the substrate. No Te atoms were found in the sample after RTA which is consistent with EDX data (not shown here). We calculated the diffusion length of Te in Si for the thermal annealing regimes applied here. According to Ref. [18] the Te diffusion coefficient in Si in the temperature range of 900–1310 °C is described by the expression

$$D_{Te} = (0.9 \pm 0.3) cm^2 s^{-1}\ exp\left[-\frac{(3.3 \pm 0.1)eV}{k_B T}\right], \tag{2}$$

where $k_B T = 0.098$ eV and 0.123 eV for 900 °C and 1200 °C, respectively. In the discussed regimes of solid-phase epitaxial recrystallization, the diffusional length is $l = \sqrt{D_{Te}(T) \cdot t}$. With the time t of the heat treatment, diffusion lengths of 20 nm and 190 nm for furnace annealing and RTA, respectively, are obtained. One can see that the estimated diffusional length in the case of RTA practically exceeds the full depth distribution of the implanted Te atoms (see Fig. 4).

Fig. 4 shows the Te concentration profiles obtained via fitting of experimental RBS/R spectra by simulated ones using the SIMNRA code. This figure also plots the concentration profile simulated using the BEAM2HD code. For the as-implanted sample, one can see a good agreement between theory (Te concentration profile simulated by BEAM2HD code) and experimental data for both the position of the maximum concentration and the value of the concentration as a function of depth. In the case of the as-implanted sample, the maximum Te concentration is ~1 × 10^{21} cm^{-3} occurring at a depth of about 90 nm. After furnace annealing, the maximum of the Te concentration shifts to about 60 nm and reaches a value of 9 × 10^{20} cm^{-3}. It should be noted that, as a result of the Te diffusion during annealing the surface Te concentration reaches up to 1 × 10^{21} cm^{-3}. After laser annealing at $W =$ 1.5 J/cm^2, an impurity plateau with a concentration of about 5 × 10^{20} cm^{-3} is formed in the depth range from the surface up to a depth of 190 nm. In the case of the samples after PLA at 2.0 and 2.5 J/cm^2, the Te concentration in the plateau region is lower (3 × 10^{20} cm^{-3}) due to the impurity diffusion towards the bulk material. As can be seen from Fig. 4, the depth of the Te distribution extends deeper into the substrate with increasing W. This can be explained by the increase of the recrystallization time due to the thicker initially molten layer (see Fig. 1). The total Te concentrations resulting from the depth profiles in Fig. 4 are given in Table 1. The reference value before annealing was found to be 1.0 × 10^{16} cm^{-2}. Table 1 shows that the total Te amount is rather unchanged, taking into account the uncertainty of ion implantation and ion beam analysis. Although, there is a slight tendency that the total number of Te atoms decreases with increasing laser energy density.

The RBS minimum yield χ is given as the ratio between the yield measured in channeling and random direction, integrated over a certain depth range. Values χ^{Si} and χ^{Te} (determined from the Si and Te signal of the implanted layer, respectively) were used to evaluate the degree of crystallinity of the implanted Si layer and the fraction of substitutional Te. The fraction f of impurity atoms on substitutional sites was calculated by the formula from Ref. [19]:

$$f = (1-\chi^{Te})/(1-\chi^{Si}). \tag{3}$$

The obtained values of χ^{Si} and f are given in Table 1 for the samples after furnace annealing and PLA. The value of χ^{Si} is equal to 24–21% for the implanted samples after PLA in contrast to 67% for the sample after furnace annealing at 900 °C. It can be seen that χ^{Si} decreases with increasing energy density in the laser pulse. For comparison, the values of χ^{Si} are ≤5% and 100% for a perfect Si crystal and fully amorphous material, respectively [19]. Thus, the degree of crystallinity of hyperdoped Si is the best after laser annealing at the maximum energy density of $W = 2.5$ J/cm^2 applied here. Based on the data from the RBS/C spectra, laser annealing also results in a significant incorporation of the Te atoms on Si lattice sites. The degree of impurity incorporation is very high (91–74%). In the case of furnace annealing at 900 °C, this value is much lower and amounts to 24% only. PLA with the smaller energy

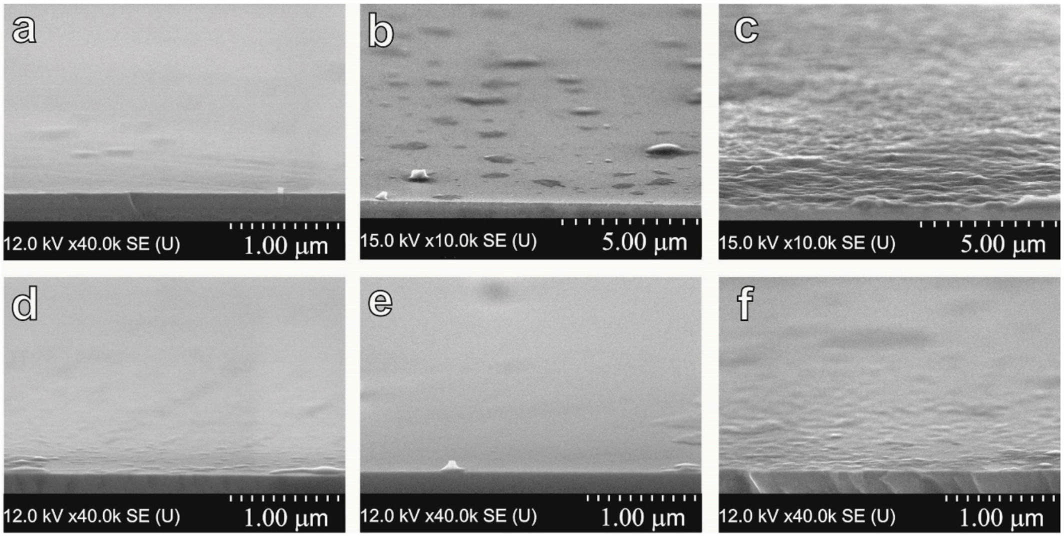

Fig. 2. SEM images of Te-implanted Si surfaces before (a) and after furnace annealing at 900 °C for 30 min (b), after rapid thermal annealing at 1200 °C for 3 min (c), after laser annealing by pulses with energy densities of 1.5 (d), 2.0 (e), 2.5 (f) J/cm^2.

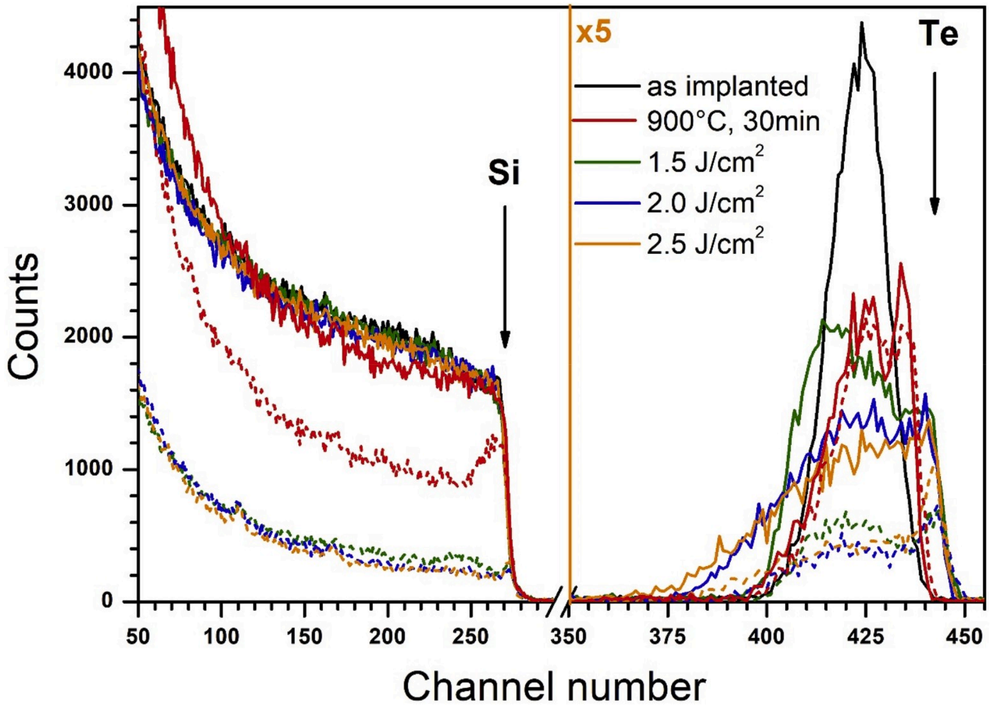

Fig. 3. RBS spectra of the Te-implanted and annealed Si samples before and after different heat treatments. Random spectra are shown as solid lines and spectra registered in channeling regime as dashed lines.

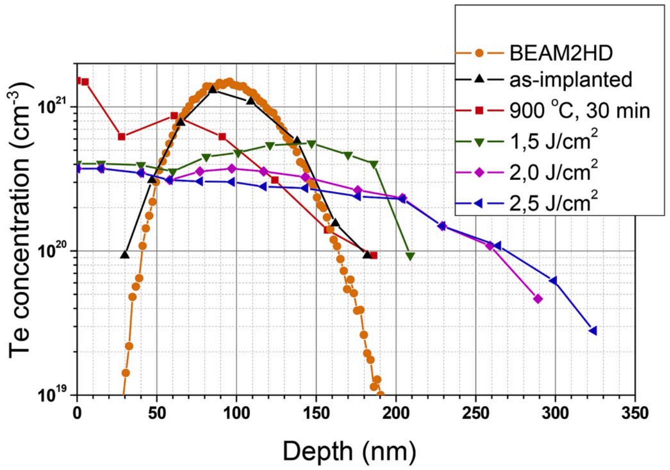

Fig. 4. Simulated and experimental Te concentration depth profiles for the implanted Si samples before and after different treatments.

Table 1
RBS minimum yield of the Si lattice, χ^{Si}, substitutional fraction of Te atoms, *f*, and total amount of Te atoms per unit area, N_I, for Te-implanted Si after furnace and pulse laser annealing.

Parameters	Samples			
	Annealing 900 °C	$W = 1.5$ J/cm^2	$W = 2.0$ J/cm^2	$W = 2.5$ J/cm^2
χ^{Si}, %	67	24	23	21
f, %	24	91	90	74
N_I, cm^{-2}	1.2×10^{16}	1.0×10^{16}	0.9×10^{16}	0.8×10^{16}

densities *W* results in more impurities being incorporated in substitutional lattice sites. In case of the most intense laser pulse with $W = 2.5$ J/cm^2, the lower Te concentration and longer duration of the recrystallization process are most likely responsible for the higher quality of the Si crystal in this case (see Table 1). In the range of the sensitivity of the RBS method (~0.01 at %) we did not register any substitutional fraction of Te atoms in Si (Fig. 3) after RTA, i. e. this fraction could be at the level of an equilibrium solubility ~10^{16} cm^{-3} [20].

Fig. 5 shows the Raman spectra for the as-implanted and annealed samples. The initial Si wafer exhibits a narrow symmetric band at 520 cm^{-1} attributed to optical phonon in Si. The implantation results in vanishing of this band as a result of full amorphization of the implanted layer. After furnace annealing, this band is registered in the RS spectrum as a consequence of restoration of the Si crystal structure. Furthermore,

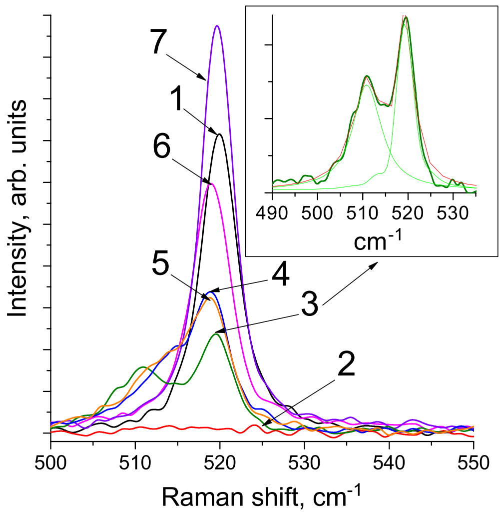

Fig. 5. Raman spectra of the Si substrate (1), Te-implanted silicon before (2) and after PLA at *W* 1.5 (3), 2.0 (4), 2.5 (5) J/cm^2, after furnace annealing at 900 °C for 30 min (6), after rapid thermal annealing at 1200 °C for 3 min (7). (For interpretation of the references to colour in this figure legend, the reader is referred to the Web version of this article.)

according to the position of this band, crystal perfection is better after RTA at 1200 °C than after furnace annealing at 900 °C. This is obviously due to the absence of impurities in the Si matrix and due to the higher temperature during annealing. Laser treatment also results in the restoration of Si with some peculiarities. In the case of the sample after PLA at $W = 1.5$ J/cm^2, the optical phonon Si band can be deconvoluted by two bands: a weak band at 511 cm^{-1} and a more intense one at 519.7 cm^{-1}. The manifestation of these bands indicates the existence of two regions with a different level of residual stress in the recrystallized Si layer. These two regions can be caused by a different recrystallization velocity due to a different dopant level and/or by differences in the remaining doping level itself (see Fig. 4). The increase of the laser energy density up to 2.0 and 2.5 J/cm^2 results in high-energy shift of the weak band, i.e. the two peaks start to merge back into one peak. This coincides with the more homogeneous Te distribution and lower concentration obtained in these cases (Fig. 4). Thus, the Raman spectra confirm that PLA results in the recrystallization of the implanted layers. However, a complete restoration of the crystalline structure of the implanted and annealed layer is not obtained. This is most likely related to the high concentration of Te incorporated into the Si lattice.

3.3. *Optical absorption investigation*

Fig. 6 shows the absorption spectra of the implanted and annealed samples in the spectral range below the fundamental absorption edge of Si (1000–2500) nm. In this range there is a minor optical absorption of the Si substrate due to the p-type doping. The amorphous as-implanted layer causes a weak absorption tail below the fundamental absorption edge. The absorption is almost back to the level of the un-implanted substrate after furnace annealing and RTA. This is consistent with the previous results which revealed almost perfectly recrystallized Si layers and Te evaporation in case of RTA as well as insignificant fraction of Te atoms in the Si lattice in case of furnace annealing. Contrary, a significant increase of the absorption at the wavelengths above 1100 nm is observed after PLA. The absorption increases from few percent in the pristine sample up to 35–65% in the implanted and pulse laser annealed samples. Additionally, this absorption increases with increasing wavelength. This is unlikely to be due to the absorption on defects in the Si lattice. Damaged or amorphous Si does not exhibit a strong absorption near Si fundamental absorption edge, and the absorption decreases rapidly with increasing wavelength [21]. Thus, the high absorption of the implanted layers after PLA can only be attributed to the high concentration of Te atoms incorporated into the Si lattice and formation of an impurity band in the Si band gap.

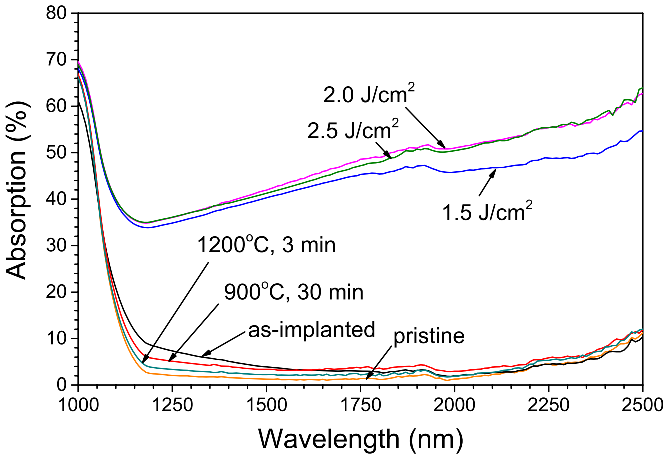

Fig. 6. Absorption spectra of pristine silicon and of Te-implanted silicon before and after annealing in different regimes. (For interpretation of the references to colour in this figure legend, the reader is referred to the Web version of this article.)

Chalcogens, such as Te and Se, are double donors in silicon. Te atoms introduce deep-donor states at $E_c - 0.20$ eV and $E_c - 0.41$ eV in the upper half of the Si band gap [18,22]. At high donor concentrations, their wave functions start to overlap resulting in broadening of the donor levels into an impurity band. The critical dopant concentration N_d for donor centres being close to one another and forming an impurity sub-band can be calculated from Ref. [23]:

$$N_d = \left(\frac{C}{\alpha_H}\right)^3, \tag{4}$$

where C is a constant with the value of 0.25, α_H is the Bohr radius approximated by

$$\alpha_H = \frac{q^2}{8\pi\varepsilon_0\varepsilon_r E_d}. \tag{5}$$

here q is the electron charge, ε_0 is the vacuum permittivity, ε_r is the permittivity of Si and E_d is the Te dopant ionization energy which is reported to be 0.14 eV [24]. Also, different values of E_d as 0.199 eV and 0.158 eV are stated in the literature [20,22,25] for a single Te atom and for a Te dimer, respectively. As single substitutional Te atoms are double donors, their critical concentration for the Mott transition in hyperdoped Si can be estimated to be in the range of 2–3 × 10^{20} cm^{-3}. According to the results of Fig. 4 and Table 1 the substitutional fraction of Te atoms exceeds this crystal level of concentration.

3.4. *Electrical characterization and photosensitivity*

The Te-hyperdoped Si samples were used to fabricate p-n photodiodes. Fig. 7 schematically presents the produced test structure. The top ring-shaped nickel electrodes were formed by magnetron sputtering followed by photolithography and plasma-chemical etching using SF$_6$. The Al contact was used as a bottom side electrode.

Fig. 7 c depicts the room-temperature current-voltage (I–V) characteristics of the test structures under dark condition at forward (Al electrode is positive one) and reverse (Al electrode is negative one) bias. Laser annealing causes significant enhancement of the conductivity in comparison with the as-implanted sample. Under a reverse bias applied voltage, a difference in the results for samples irradiated at different energy density of laser pulses is revealed. The sample irradiated at $W =$ 1.5 J/cm^2 exhibits the best conductivity at voltages $|U|<4$ V. At $|U|>4$ V, the conductivity is higher for the spot irradiated at $W = 2.0$ J/cm^2.

According to Fig. 8, the conductivity of Te-hyperdoped Si layers increases under the illumination. The incident light spot of a halogen lamp

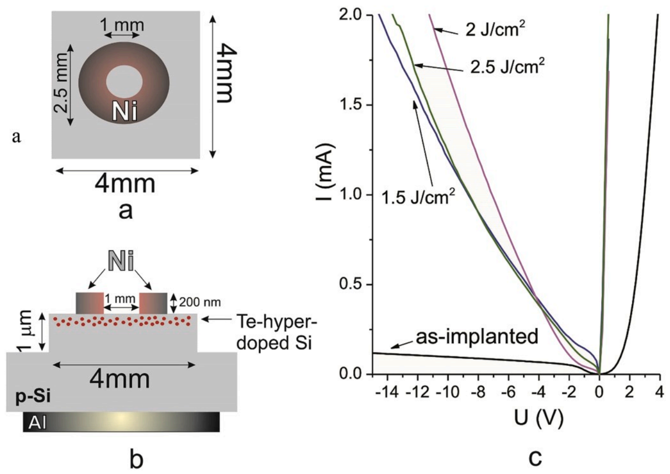

Fig. 7. Top view (a) and cross-section (b) schemes of the Te-hyperdoped photodiode test structure. Part (c) shows the current voltage characteristics measured at room temperature under dark condition.

(3000 K) was used to study the photoresponse. The illumination was carried out using the full spectrum of the lamp and using only the IR spectral range (>1 μm) with a virgin Si wafer as a cut filter. The photoresponse was characterized by the ratio of currents measured under illumination condition (I_L) and under dark condition (I_0). The best photoresponse is registered for the laser-annealed sample at $W = 2.0$ J/cm^2 and reverse bias applied voltage less than 4 V. Under the reverse bias applied voltage in the range of (−4; −12) the sample irradiated at $W = 2.5$ J/cm^2 exhibits the best photosensitivity. It corresponds to the better restoration of the crystalline structure of the implanted and annealed layer with the increase of laser energy density up to 2.0 and 2.5 J/cm^2 as shown in Fig. 5 and discussed above. Fig. 4 depicts a sharper decrease of the Te concentration at depths deeper than 200 nm for the sample annealed with the energy density of 2.0 J/cm^2. The impurity concentration at this depth is insufficient to form the impurity band as estimated earlier. Instead, deep levels inherently reduce the non-radiative carrier lifetime and increase the probability for Shockley-Read-Hall recombination [26]. Both of these effects are considered detrimental to semiconductor device performance.

Further efforts must be paid to increase the photodetector efficiency. This can be achieved by designing optimal top and back electrodes to enhance carrier-collection efficiency as well as by application of an antireflection coating. In addition, top side or both sides passivation (by SiO_2 layers) with a back surface point contact must be used to reduce the carrier surface recombination. The diode characteristics and device responsivity depend strongly on the processing conditions including doping levels of the substrate and implanted layer, laser energy intensity and regimes of thermal treatment.

Moreover, in order to convert the absorbed subband gap photons effectively into electronic carriers at room temperature, the intermediate band, introduced by hyperdoping, must be isolated from both the valence band and conduction band. The higher tellurium concentration N_d corresponds to a broader impurity band [27].

$$\Delta E_{IB} = \frac{q^2 N_d^{\frac{1}{3}}}{4\pi\varepsilon_0\varepsilon r}. \tag{6}$$

When the impurity band is broad enough that it practically merges at room temperature with the conduction band, electrons are no longer delocalized on the donor levels and become free carriers. In this case the ratio of thermal-to-optical carrier generation is sufficiently high to screen a measurable photocurrent arising from the transition from the impurity band to the conduction bond. It causes a strong increase of a dark current in detectors.

4. Conclusions

In summary, different types of thermal treatment were tested to form Te-hyperdoped silicon layers with good crystallinity and absorptive properties. RTA at the chosen regime (1200 °C, 3 min) results in full impurity loss and destruction of the Si surface. Equilibrium furnace annealing (900 °C, 30 min) leads to a relatively high degree of recrystallization, but also to high diffusion of Te atoms towards the surface and surface Te agglomeration. Consequently, in the case of this sample, the IR absorption increase was only 4% compared to virgin crystalline silicon.

It is shown that strongest effects are obtained with PLA, whereby the structural and absorption properties depend on the energy density of the laser pulses W (1.5–2.5 J/cm^2). Based on the RBS/C and Raman spectroscopy data, it can be concluded that the degree of recrystallization was improved with W. On the other side, the ratio of substitutional Te atoms at the Si lattice sites to the total amount of embedded Te atoms decreases from 91% to 74% with the increase of W from 1.5 to 2.5 J/cm^2. Additionally, the maximum depth of the Te distribution also increases with W, which can be related to the longer time of melting. The laser pulse treatment results in an increase of the IR absorption up to 35–65%, which tends to increase with increasing energy density.

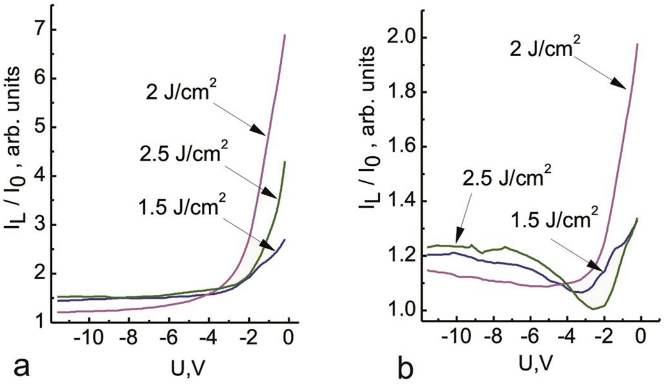

Fig. 8. Ratio of currents measured under illumination and dark conditions versus the applied voltage. The illumination was carried out using the full spectrum of the halogen lamp (a) and (b) using only the IR light passed through virgin Si substrate.

Laser annealing of Te-implanted silicon layers results in an enhancement of the electrical conductivity. The samples irradiated at $W = 1.5$ J/cm^2 and $W = 2.0$ J/cm^2 are characterized by the highest conductivity at reverse bias applied voltage $|U| < 4$ V and $|U| > 4$ V, respectively. The best photoresponse is registered for the sample after laser annealing at $W = 2.0$ J/cm^2 and at reverse applied bias voltage $|U| < 4$ V. The sample irradiated at $W = 2.5$ J/cm^2 exhibits the best photosensitivity under the reverse applied bias voltage at the range of (−4; −12). Thus, both factors (dopant activation and degree of recrystallization) play an important role on IR absorption and photoresponse. The revealed peculiarities are undoubtedly of interest in the manufacture of Si-based IR photodectors.

Declaration of competing interest

The authors declare that they have no known competing financial interests or personal relationships that could have appeared to influence the work reported in this paper.

Acknowledgments

The work was carried out with a partial financial support from the Ministry of Education and Science of the Russian Federation in the framework of Increase Competitiveness Program of NUST "MISIS". The authors acknowledge the support of the Erasmus + Program of the EU.

References

[1] J.E. Carey, C.H. Crouch, M. Shen, E. Mazur, Visible and near-infrared responsivity of femtosecond-laser microstructured silicon photodiodes, Opt. Lett. 30 (2005) 1773–1775, https://doi.org/10.1364/OL.30.001773.

[2] B.P. Bob, A. Kohno, S. Charnvanichborikarn, J.M. Warrender, I. Umezu, M. Tabbal, J.S. Williams, M.J. Aziz, Fabrication and subband gap optical properties of silicon supersaturated with chalcogens by ion implantation and pulsed laser melting, J. Appl. Phys. 107 (2010), 123506, https://doi.org/10.1063/1.3415544.

[3] E. Schibli, A.G. Milnes, Deep impurities in silicon, Mater. Sci. Eng. 2 (1967) 173–180, https://doi.org/10.1016/0025-5416(67)90056-0.

[4] Z.A.Y. Abdalla, M.Y.A. Ismail, E.G. Njoroge, T.T. Hlatshwayo, E. Wendler, J. B. Malherbe, Migration behaviour of selenium implanted into polycrystalline 3C–SiC, Vacuum 175 (2020), 109235, https://doi.org/10.1016/j.vacuum.2020.10.

[5] R.-D. Chang, H.-C. Liao, C.-M. Tai, Anomalous rapid diffusion of phosphorus caused by heavily implanted carbon in pre-amorphized ultrashallow junctions, Vacuum 140 (2016) 161, https://doi.org/10.1016/j.vacuum.2016.10.003, 164.

[6] Y. Berencén, S. Prucnal, F. Liu, I. Skorupa, R. Hübner, L. Rebohle, S. Zhou, H. Schneider, M. Helm, W. Skorupa, Room-temperature short-wavelength infrared Si photodetector, Sci. Rep. 7 (2017) 43688. https://doi:10.1038/srep43688.

[7] W. Shockley, H.J. Queisser, Detailed balance limit of efficiency of p–n junction solar cells, J. Appl. Phys. 32 (1961) 510–519, https://doi.org/10.1063/1.1736034.

[8] A. Luque, A. Martí, Increasing the efficiency of ideal solar cells by photon induced transitions at intermediate levels, Phys. Rev. Lett. 78 (1997) 5014–5017, https://doi.org/10.1103/PhysRevLett.78.5014.

[9] H.-J. Gossmann, C.S. Rafferty, P. Keys, Junctions for deep sub-100 nm MOS: how far will ion implantation take us? Mater. Res. Soc. Symp. 610 (2000) https://doi.org/10.1557/PROC-610-B1.2. B1.2.1–B1.2.10.

[10] H.J. Gossmann, F.C. Unterwald, H.S. Luftman, Doping of Si thin films by low temperature molecular beam epitaxy, J. Appl. Phys. 73 (1993) 8237–8241, https://doi.org/10.1063/1.353441.

[11] E. Ertekin, M.T. Winkler, D. Recht, A.J. Said, M.J. Aziz, T. Buonassisi, J. C. Grossman, Insulator-to-Metal transition in selenium-hyperdoped silicon: observation and origin, Phys. Rev. Lett. 108 (2012), 026401, https://doi:10.1103/PhysRevLett.108.026401.

[12] S. Zhou, F. Liu, S. Prucnal, K. Gao, M. Khalid, C. Baehtz, M. Posselt, W. Skorupa, M. Helm, Hyperdoping silicon with selenium: solid vs. liquid phase epitaxy, Sci. Rep. 5 (2015) 8329. https://doi:10.1038/srep08329.

[13] M. Wang, Y. Berencén, E. García-Hemme, S. Prucnal, R. Hübner, Ye Yuan, Chi Xu, L. Rebohle, R. Böttger, R. Heller, H. Schneider, W. Skorupa, M. Helm, Shengqiang Zhou, Extended infrared photoresponse in Te-Hyperdoped Si at room temperature, Phys. Rev. Applied. 10 (2018), 024054.

[14] M. Wang, R. Hubner, C.X.Y. Xie, Y. Berencén, R. Heller, L. Rebohle, M. Helm, S. Prucnal, S. Zhou, Thermal stability of Te-hyperdoped Si: atomic-scale correlation of the structural, electrical and optical properties, Phys. Rev. Mater. 3 (2019), 044606, https://doi:10.1103/PhysRevMaterials.3.044606.

[15] G.D. Ivlev, E.I. Gatskevich, Optical–pyrometric diagnostics of the state of silicon during nanopulsed laser irradiation, Tech. Phys. 57 (2012) 803–806.

[16] M. Mayer, SIMNRA User's Guide, Max-Planck-Institute fur Plasmaphysik, Garching, 1997.

[17] A.F. Komarov, F.F. Komarov, P. Zukowski, C. Karwat, A. Shukan, Simulation of the process of high dose ion implantation in solid targets, Nukleonika 44 (1999) 363–368.

[18] H. Stümpel, M. Vorderwülbecke, J. Mimkes, Diffusion of selenium and tellurium in silicon, Appl. Phys. A 46 (1988) 159–163.

[19] L.C. Feldman, J.W. Mayer, S.T. Picraux, Materials Analysis by Ion Channeling: Submicron Crystallography, Academic Press, New York, 1982.

[20] P. Wagner, C. Holm, E. Sirtl, R. Oeder, W. Zulehner, in: P. Grosse, Vieweg (Eds.), Festkorperprobleme: Advances in Solid State Physics, 24, 1984, p. 191. Braunschweig.

[21] W. Wesch, E. Glaser, G. Götz, H. Karge, R. Prager, Correlation between structural defects and optical porperties in ion-implanted silicon, Phys. Status Solidi 65 (1981) 225, https://doi.org/10.1002/pssa.2210650126.

[22] R. Shaub, G. Pensl, M. Schulz, C. Holm, Donor states in tellurium-doped silicon, Appl. Phys. A 34 (1984) 215–218, https://doi.org/10.1007/BF00616575.

[23] N.F. Mott, Metal-insulator transition, Contemp. Phys. 14 (1973) 401.

[24] G.E. Brock, Metallurgy of Advanced Electronic Materials, 19, 1963. New York.

[25] K. Sánchez, I. Aguilera, P. Palacios, P. Wahnón, Formation of a reliable intermediate band in Si heavily coimplanted with chalcogens (S, Se, Te) and group III elements (B, Al), Phys. Rev. B 82 (2010), 165201, https://doi.org/10.1103/PhysRevB.82.165201.

[26] W. Shockley, W.T. Read, Statistics of the recombinations of holes and electrons, Phys. Rev. 87 (1952) 5–12, 10.1103/PhysRev.87.835.

[27] E.F. Schubert, Doping III-V Semiconductors, Cambridge University Press, 1993, p. 632, https://doi.org/10.1017/CBO9780511599828.